Nanoscale Research Letters

NANO EXPRESS Open Access

Co/CoP Nanoparticles Encapsulated Within N, P-Doped Carbon Nanotubes on Nanoporous Metal-Organic Framework Nanosheets for Oxygen Reduction and Oxygen Evolution Reactions

Xinxin Yang[1], Hongwei Mi[1], Xiangzhong Ren[1], Peixin Zhang[1,2] and Yongliang Li[1,2*]

Abstract

Herein, Co/CoP nanoparticles encapsulated with N, P-doped carbon nanotubes derived from the atomic layer deposited hexagonal metal-organic frameworks (MOFs) are obtained by calcinations and subsequent phosphating and are employed as electrocatalyst. The electrocatalytic performance evaluations show that the as-prepared electrocatalyst exhibits an overpotential of 342 mV at current density of 10 mA cm^{-2} and the Tafel slope of 74 mV dec^{-1} for oxygen evolution reaction (OER), which is superior to the most advanced ruthenium oxide electrocatalyst. The electrocatalyst also shows better stability than the benchmark RuO_2. After 9 h, the current density is only decreased by 10%, which is far less than the loss of RuO_2. Moreover, its onset potential for oxygen reduction reaction (ORR) is 0.93 V and follows the ideal 4-electron approach. After the stability test, the current density of the electrocatalyst retains 94% of the initial value, which is better than Pt/C. The above results indicate that the electrocatalyst has bifunctional activity and excellent stability both for OER and ORR. It is believed that this strategy provides guidance for the synthesis of cobalt phosphide/carbon-based electrocatalysts.

Keywords: Transition metal phosphide, Metal-organic frameworks, Bifunctional electrocatalyst

Introduction

The development of modern society depends on energy supply to a large extent, but with environmental problems induced by the burning of fossil fuels and the aggravation of energy shortage, it is necessary to find new conversion systems or renewable energy [1–4]. Fuel cells and metal-air batteries are considered to be promising energy systems; however, their poor energy conversion efficiency and short life span are the main bottlenecks that limit their widespread use [5–9]. These deficiencies are primarily on account of the inherent sluggish kinetics of the oxygen evolution reaction (OER) and oxygen reduction reaction (ORR) [10–13]. Especially, OER plays a very important role in metal-air batteries and water splitting. However, the slow kinetics of it usually result in low reaction rates and high electrode overpotential, hindering the development such energy systems. Currently, the most accepted theory explains the OER process under alkaline conditions is as follows:

$$M + OH \rightarrow M\text{–}OH + e^- \quad (1)$$

$$M\text{–}OH + OH^- \rightarrow M\text{–}O^- + H_2O \quad (2)$$

* Correspondence: liyli@szu.edu.cn
[1]College of Chemistry and Environmental Engineering, Shenzhen University, Shenzhen 518060, Guangdong, People's Republic of China
[2]Guangdong Flexible Wearable Energy Tools Engineering Technology Research Centre, Shenzhen University, Shenzhen 518060, Guangdong, People's Republic of China

$$M\text{–}O^- \rightarrow M\text{–}O + e^- \quad (3)$$

$$2M\text{–}O \rightarrow 2M + O_2 \quad (4)$$

ORR as a cathode reaction of a fuel cell is a key factor restricting the efficiency of the cell. During the reaction, a variety of intermediate oxygen species are generated, and the reaction process is relatively complicated. Under alkaline conditions, there are two reaction modes:

$2e^-$ path:

$$O_2 + H_2O + 2e^- \rightarrow HO_2 + OH_2^- \quad (5)$$

$$HO_2^- + OH^- + 2e^- \rightarrow 3OH^- \text{ or } HO_2^- + OH^- + 2e^- \rightarrow 3OH^- \quad (6)$$

$4e^-$ path:

$$O_2 + 2H_2O + 4e^- \rightarrow 4OH^- \quad (7)$$

Therefore, the exploration of inexpensive, highly efficient, and durable electrocatalysts is necessary to promote the practical application of these renewable resources [14, 15]. At present, precious metals are considered to be the most active electrocatalysts such as Pt, Ru, Ir, and their alloys, but high cost, scarcity, and lack of bifunctional catalysis have seriously hindered their commercialization [16–20]. Therefore, the pursuit of bifunctional, stable and inexpensive electrocatalysts is urgently needed for the demand of commercialization. Transition metal phosphides (TMPs) are promising alternative candidates of which Co^{2+} in Co_xP_y provides OH^- adsorption center and converts it into products, while negative P center accelerates OH^- adsorption to Co^{2+}, resulting in low cost, excellent performance, high efficiency, and good durability [21–24]. Many researchers have made great efforts to design CoP_x nanostructures with diverse and high electrocatalytic activity. Since the activity depends largely on their surface properties, many research focused on the structure engineering of electrocatalysts to expose catalytic active sites as much as possible, for example various nanostructured TMPs, including nanoparticles [25, 26], nanowires [27, 28], nanotubes [29, 30], and nanorods [31, 32] are developed and most of them showed good electrocatalytic performance. There have been many reports that high-efficiency and strong cobalt-based materials were considered as a promising OER electrocatalyst due to its high efficiency, high abundance, and good stability in recent years. Cobalt phosphide (CoP) is one of the TMPs families. Due to the novel characteristics of CoP, its application in battery electrocatalysis and photocatalysis has received extensive attention. It provides a large number of active sites for electrochemical reaction to promote electrocatalytic activity [33]. CoP not only solves the problems of insufficient reserves, high price, and poor stability of Ru and Ir electrocatalysts, but also has good catalytic performance for OER [34, 35]. In addition, CoP has neutral alkali resistance and is advantageous for electrochemical stability. However, the conductivity of CoP is poor, which seriously affects its electrocatalytic activity [36].

Metal-organic frameworks (MOFs) are a series of adjustable organic-inorganic hybrid materials with adjustable structures [37, 38]. In short, metal ions are uniformly dispersed at the atomic level in the MOFs precursor, and the presence of organic ligands in the MOFs enables them to be calcined into various carbon materials without introducing an external carbon source [39]. As a general precursor for the preparation of TMPs, MOFs compounds have been extensively studied by reason of their large specific surface area, high porosity, and structural coordination [40, 41]. In general, MOFs carbonization process requires high temperature calcination, which will damage the original MOFs structure and cause agglomeration of the metal center [42]. Direct use of MOFs as an electrocatalyst can utilize its good structure, but their stability is relatively low, and catalytic activity is poor, especially under strong alkaline and acidic solution conditions [43, 44]. If reasonably designed, the hybrid electrocatalyst combining TMPs and MOFs not only enhances the intrinsic catalytic activity but also utilizes the well-defined porous structure of MOFs. More importantly, the center of the coordinated unsaturated metal MOFs is more favorable for adsorption oxygen-containing substances, which will further enhance catalytic performance [45].

Herein, we report the preparation of nanotubes (CNTs) derived from N-doped porous MOFs nanosheets (NPM) via atomic layer deposition (ALD) techniques, with Co/CoP nanoparticles encapsulated at the tip of the nanotubes. The controlled portion of the Co-MOFs creates a Co/CoP species during the phosphating process, resulting in a hybrid nanostructure that have a large specific surface area. The as-prepared product is used as electrocatalyst, exhibiting a bifunctional feature in electrochemical performance for both OER and ORR. Its onset potential was 0.93 V for ORR while the overpotential was about 342 mV with the Tafel slope of 74 mV dec^{-1} for OER. Moreover, the electrocatalyst also showed excellent stability for both reactions.

Methods

Materials

Potassium hydroxide (KOH), 2-methylimidazole ($C_4H_6N_2$), sodium hypophosphite (NaH_2PO_2), and zinc nitrate hexahydrate ($Zn(NO_3)_2{\cdot}6H_2O$) were purchased from Shanghai Macklin Biochemical Technology Co.,

Ltd. Cobaltocene ($(\eta5\text{-}C_5H_5)_2Co$) was purchased from Suzhou Fornano Co., Ltd. All of the above chemicals are analytically pure. Nafion solution (5 wt%) was purchased from Shanghai Hesen Co., Ltd.

Synthesis of Electrocatalysts

First, 90 mL of deionized water including 0.33 g of zinc nitrite hexahydrate was slowly added to another prepared solution of 90 mL of deionized water including 0.985 g of 2-methylimidazole, then stirred continuously for 24 h at 25 °C. This mixture was centrifuged with ethyl alcohol absolute several times and dried at 70 °C in ambient air, the finally obtained white powder denoted as NPM.

The electrocatalyst (denoted as NPMCNT) was deposited by using equipment of KEMICRO PEALD-200A (Kemin Co. Ltd, China). During the PE-ALD process, Cobaltocene ($CoCp_2$) was used as Co source and oxygen plasma (O_2, 99.999%) was used as O source. This sedimentary process was deposited at 200 °C in a vacuum reaction chamber and argon (Ar, 99.999%) as the carrier gas was used to purge excess sources. The Co source temperature was 100 °C. The second source (oxygen plasma) was maintained at 25 °C. The deposition process consists of 200 cycles and each cycle consists of 4 steps: Co source, Ar, oxygen plasma, and Ar. The dose times of Co source and oxygen plasma were 3 and 20 s respectively, and the Ar purge time was 50 s. The obtained powder was annealed at 925 °C for 2 h under N_2 with the heating rate of 2 °C min^{-1}. The acquired product was named NPMCNT.

The 10 mg NPMCNT electrocatalyst obtained above was placed upstream of the tube furnace, and 300 mg of sodium hypophosphite was placed downstream of the tube furnace, and then annealed at 350 °C for 2 h under N_2 with the heating rate of 2 °C min^{-1}. The acquired product was named NPMCNT-300. The NPMCNT-50, NPMCNT-100, NPMCNT-200, and NPMCNT-400 were prepared using the same procedure but the sodium hypophosphite amount was changed as 50, 100, 200, and 400 mg, respectively.

Physical Characterization

The crystallite structure was acquired by X-ray powder diffraction (XRD, Empyrean, PANalytical) with Cu Kα radiation. The morphology was confirmed by the field emission scanning electron microscope (FESEM, JSM-7800F). The microstructure was observed by transmission electron microscope (FETEM, JEM-200). The element distribution was measured by energy dispersive X-ray spectroscopy (EDS, JEM-F200). The relationship of the bond energy was collected by X-ray photoelectron spectroscopy (XPS, K-Alpha+). Nitrogen adsorption–desorption isotherms were collected on a BELSORP-max II instrument.

Electrochemical Measurements

The 5 mg of the NPMCNT-300 electrocatalyst was added into the mixed solution containing 100 μm Nafion (5 wt%, DuPont) and 1 mL ethyl alcohol absolute, then treated with an ultrasound for 30 min to form a well-proportioned mixture. Twelve microliter of the homogeneous mixture was dropped several times onto pre-polished glassy carbon electrode, and then dried it naturally at room temperature.

All the electrochemical measurements were measured by CHI760E workstation (China) with three-electrode system. The ORR and OER activities were investigated using a rotating ring-disk electrode (RRDE, Φ_d = 4 mm, $\Phi_{Pt\ ring}$ = inner/outer-ring diameter 5.0/7.0 mm, ALS, Japan) in 0.1 M KOH. The smooth carbon electrode with deposited electrocatalyst, the platinum wire, and the Ag/AgCl electrode were served as working, counter, and reference electrodes, respectively. The linear sweep voltammogram (LSV) technique was used to test the electrochemical catalytic activity with voltage range 1.1653~0.1653 V (vs. RHE), with rotation speed of electrode 1600 rpm and the scan rate of 5 mV s^{-1} in 0.1 M KOH electrolyte. All potential values convert to that of a reversible hydrogen electrode (RHE) by the following formula:

$$E_{RHE} = E_{Ag/AgCl} + 0.0591 \times pH + 0.197\ (V). \quad (8)$$

At different various rotational speeds (400, 625, 900, 1225, 1600, and 2025 rpm), the value of the transfer electron number (n) of the LSV curve during the ORR obtained by RDE can be calculated by the following Koutecky-Levich (K-L) equation:

$$\frac{1}{j} = \frac{1}{j_k} + \frac{1}{j_d} = \frac{1}{nFKC_{O_2}} + \frac{1}{B\omega^{1/2}} \quad (9)$$

$$B = 0.2nFC_{O_2}D_{O_2}^{1/3}V^{-1/6} \quad (10)$$

where j is the measured current density, j_k is the estimated kinetic limiting current densities, n is the overall number of electrons transferred per oxygen molecule. F is the Faraday constant (F = 96,485 C mol^{-1}), and ω is the angular velocity of the disk ($\omega = 2\pi N$, N is the linear rotation speed), C_{O_2} is the bulk concentration of O_2 in the electrolyte (0.1 M KOH, 1.2×10^{-6} mol cm^{-3}), D_{O_2} is the diffusion coefficient of O_2 in the electrolyte (1.9×10^{-5} cm^2 s^{-1}), ν is the kinematic viscosity of the electrolyte (0.01 cm^2 s^{-1}), k is the electron transfer rate constant. The constant 0.2 is generally accepted when the rotating speed is presented in rpm. The electron transfer

number (n) and the yield of H_2O_2 tested by the RRDE measurement and calculated by the ring and disk currents by the following formulas:

$$n = 4 \times \frac{I_{\text{disk}}}{I_{\text{disk}} + I_{\text{ring}}/N} \tag{11}$$

$$\text{HO}_2^-(\%) = 100 \times \frac{2I_{\text{ring}}/N}{I_{\text{disk}} + I_{\text{ring}}/N} \tag{12}$$

where I_{ring} and I_{disk} are the ring and the disk currents, respectively. N value was adjusted to 0.43 using a $[Fe(CN)_6]^{4-/3-}$ redox couple.

The electrochemical active surface area (ECSA) was measured at various scanning rates (5–35 mV s^{-1}) and 0~0.15 V (vs. Ag/AgCl) by cyclic voltammetry (CV) measurement.

Results and Discussion

XRD and SEM Characterization

In Fig. 1a, typical patterns of Co (PDF no.15-0806) and CoP (PDF no.29-0497) are shown in the XRD patterns of NPMCNT composites under different phosphorus source intakes. It is worth noting that the intake of different phosphorus sources during phosphating process will lead to the formation of different products. When the phosphorus source was 50, 100, and 200 mg, it was obvious that the characteristic peak of Co_2P at 40.7° appeared. However, when the phosphorus source intake was increased to 300 and 400 mg, the characteristic peak of Co_2P was disappeared. Therefore, the Co/CoP hybrid was obtained when using the latter mass of phosphorus source. The characteristic peaks displayed between 20° and 30° are due to the carbon clothes formed after MOFs calcination. It can be observed in Fig. 1b, NPM presents a hexagonal sheet structure after pyrolysis at high temperature and Fig. 1 c shows that CNTs were generated evenly on the surface of NPM sheet. Herein, according to our previous work [1], CoOx was deposited by ALD on the surface of NPM at 200 °C, which is reduced to Co by carbon at 925 °C and nanotubes are grown. When the phosphorus source intake was 400 mg, the nanotubes were already bonded together instead of being individual distribution as shown in Fig. 1d.

TEM Characterization

TEM observation shows the entire view of the entire NPMCNT-300. Obviously, the bulk morphology of MOFs was preserved, and a large number of nanotubes were clearly visible at the edges, as well as the nanoparticles are encapsulated in the carbon nanotubes (Fig. 2a). The high-resolution TEM in Fig. 2b further proves the nanoparticles encapsulated at the tip of carbon nanotubes. Co nanoparticles will catalyze the derivation of CNTs from MOFs, which can improve the conductivity of the entire hybrid structure. And few layer of graphitic carbon layer

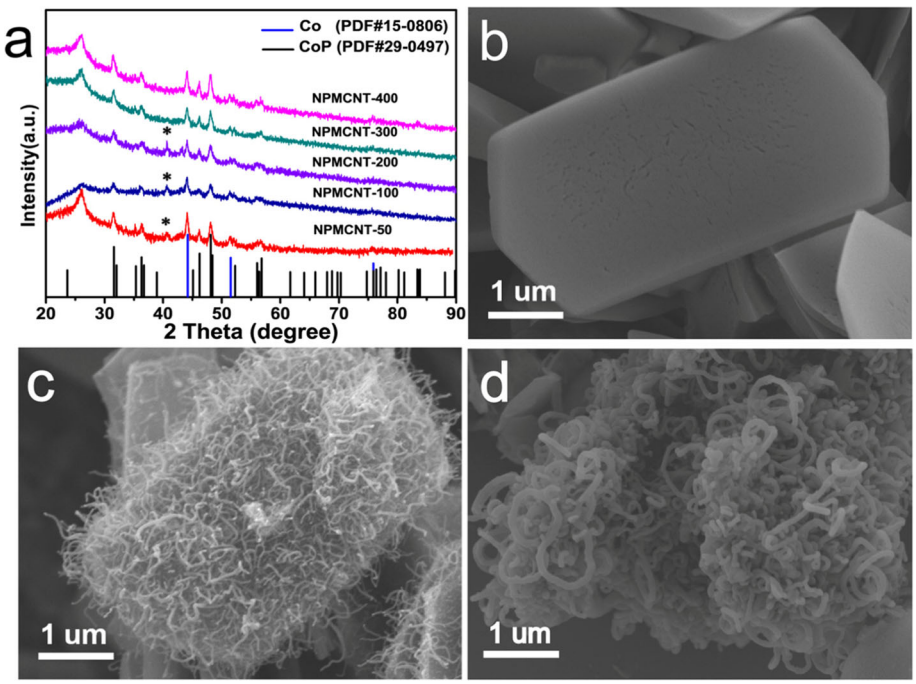

Fig. 1 a The XRD patterns. SEM images of **b** NPM, **c** NPMCNT-300, **d** NPMCNT-400

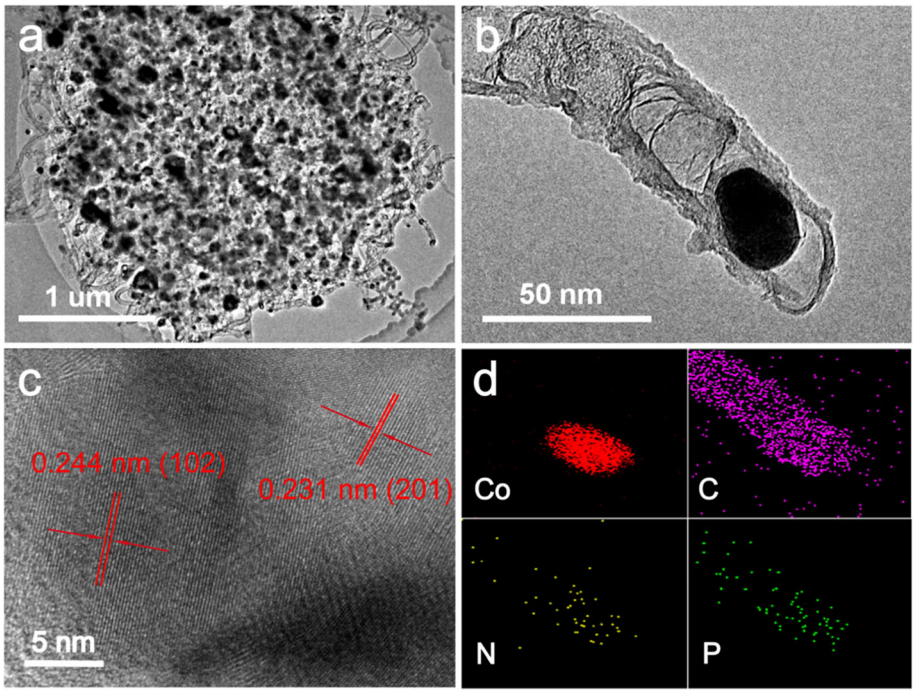

Fig. 2 TEM images of the **a** NPMCNT-300 electrocatalyst and **b** CoP nanoparticles encapsulated in the CNT tip derived from the carbon layer. **c** HRTEM image of NPMCNT-300 electrocatalyst. **d** EDS elemental mapping corresponding to the area in TEM image of NPMCNT-300 electrocatalyst

can prevent the embedded Co and CoP nanoparticles from corrosion, aggregation, and oxidation during the electrocatalytic processes, which results in excellent durability and stability in harsh environments. In addition, the N-doped CNTs structure derived from MOFs provides an effective way to adjust the electronic structure of the electrocatalyst, thereby promoting catalytic performance. The plane spacing in Fig. 2c is determined to be 0.244 and 0.231 nm, identifying with the (102) and (201) crystal plane of the CoP nanoparticles, respectively. The EDS analysis (Fig. 2d) further confirmed that the nanoparticles were encapsulated at the tip of the CNTs, and the mapped image also shows that P was not only present in the CoP nanoparticles but also in the CNTs. The N-doped carbon-supported nanomaterials can be obtained from organic monomers (2-methylimidazole) by heat treatment without using any external source. For the phosphorus doping, the NaH_2PO_2 is as the phosphorus source and will dope into the carbon structure by heat treatment at 350 °C. In this work, doping of different heteroatoms can modify the chemical structure and electronic structure of the electrocatalyst, so that the surface of the derived nanotubes will have more catalytically active sites. Some reports indicated that carbon defects can generate active sites by adjusting the electronic structure and surface polarity of carbon, thereby improving the electrocatalytic performance. Therefore, carbon-based cobalt phosphide nanocomposites doped with multiple heteroatoms have more excellent electrocatalytic activity [46–48].

XPS Characterization

The species and elemental composition of the NPMCNT-300 electrocatalyst were determined by XPS, Fig. 3 a displays the existence of Co, P, N, C, and O elements in the survey spectrum. The Co 2p spectrum in Fig. 3b shows peaks centered on 778.6 and 781.6 eV connected to Co $2p_{3/2}$, 793.9, and 797.5 eV are attributed to Co $2p_{1/2}$, respectively. The peaks centralized at 778.9 eV and 793.9 eV are associated with Co^{3+}, other peaks were centered at 781.6 eV and 797.5 eV are connected to Co^{2+}. In addition, the strong satellite peaks centered on 786.2 and 803 eV are attributed to the vibration of Co^{3+} [21, 49–51]. As shown in Fig. 3c in the P 2p spectrum, the band of 129.8 eV is connected to P $2p_{3/2}$, while the band of 130.3 eV corresponds to P $2p_{1/2}$. Two peaks of 129.8 and 130.3 eV are correlated to CoP. Another peak at 134.0 eV is attributed to P–C, while the peak located at 134.8 eV is associated with P–O [41, 52, 53]. These results confirmed that NaH_2PO_2 acts as a phosphorus source for doping into CNTs and forming CoP. In Fig. 3d, the C1 s spectrum divided into four peaks (284.7, 285.2, 286.4, and 288.4 eV). The strong peak centralized at 284.7 eV corresponding with sp^2 C = C energy of

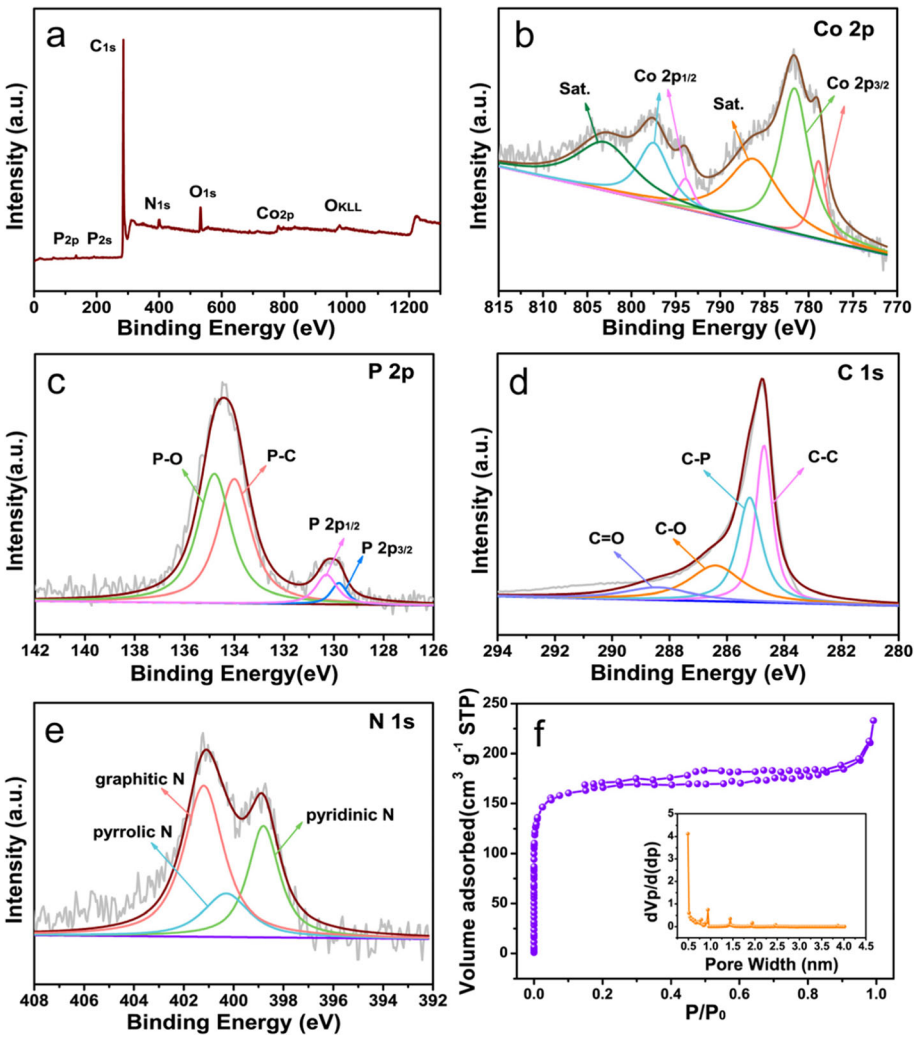

Fig. 3 **a** XPS spectrum of NPMCNT-300 electrocatalyst. **b** Co 2p XPS spectrum of NPMCNT-300 electrocatalyst. **c** P 2p XPS spectrum of NPMCNT-300 electrocatalyst. **d** C1 s XPS spectrum of NPMCNT-300 electrocatalyst. **e** N1 s XPS spectrum of NPMCNT-300 electrocatalyst. **f** N_2 adsorption–desorption isotherms and the corresponding pore size distribution curves

pyrolytic graphite. The peak (285.2 eV) is associated with the C–P matrix to the sp^2 C bonded to P in the aromatic ring. Moreover, the peak of 286.4 eV is assigned to the C–O band. In addition, the peak of 288.4 eV is associated with C = O [30, 50, 54, 55]. The high-resolution N1 s peak of NPMCNT-300 is shown in Fig. 3e and it can be fitted by three peaks located at 398.8, 400.3, and 401.2 eV identifying with pyridinic N, pyrrolic N, graphitic N, respectively [56, 57]. The above XPS results demonstrate that P and N are doped into the defect sites of the CNTs by replacing the O or C atoms.

Brunauer–Emmett–Teller (BET) Characterization

The nitrogen adsorption/desorption isotherms of NPMCNT-300 is shown in Fig. 3f. It is worth mentioning that the isotherms show a type-IV hysteretic loop, which demonstrates the presence of numerous mesoporous/microporous in NPMCNT-300 [58, 59]. And the BET surface area value of NPMCNT-300 electrocatalyst is 641 m^2 g^{-1}, these consequences show that the presence of nanotubes during the synthesis of NPMCNT-300 can greatly increase the specific surface area and pore volume of the electrocatalyst. This unique porous structure with large specific surface area is thought to be important for oxygen absorption and transportation of reactant molecules and exposure of the most active substances.

Electrocatalytic Performance and Discussion

The electrocatalytic activity was tested using a three-electrode system for ORR. In Fig. 4a, the LSV curves were examined in an O_2-saturated electrolyte. The onset potentials of NPMCNT, NPMCNT-50, NPMCNT-100, NPMCNT-200, NPMCNT-300, and NPMCNT-400 are

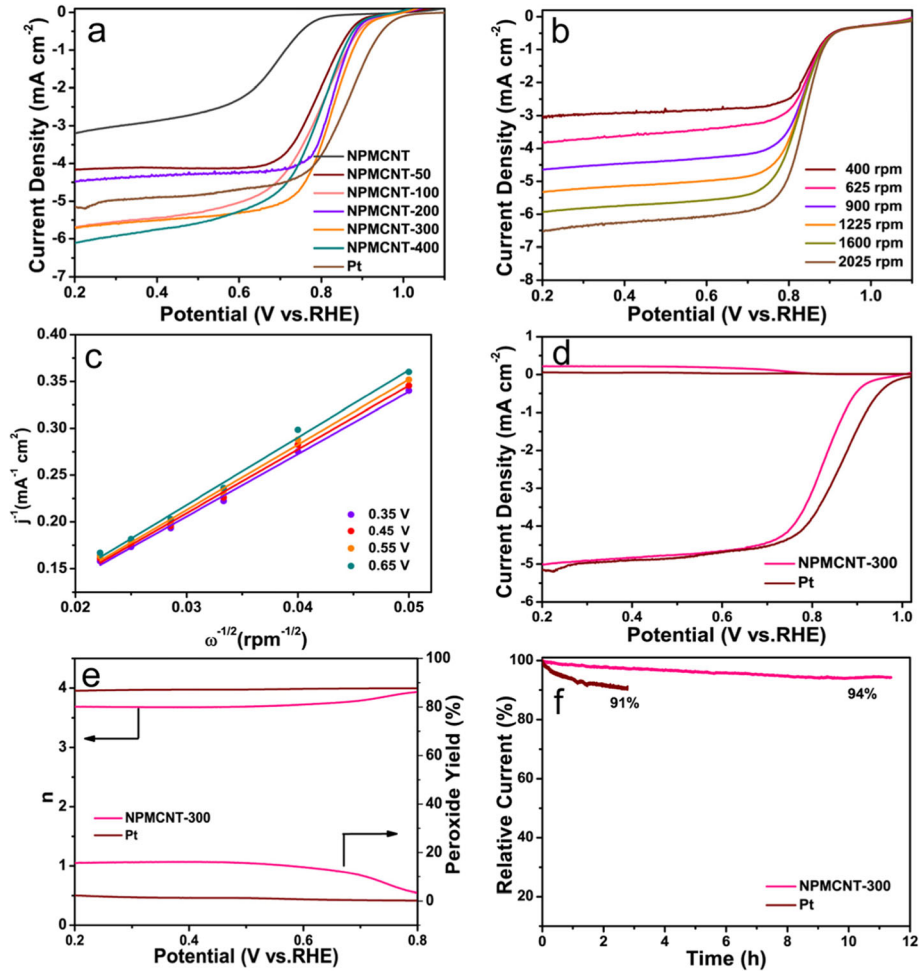

Fig. 4 **a** Linear sweep voltammetry curves of the NPMCNT, NPMCNT-50, NPMCNT-100, NPMCNT-200, NPMCNT-300, NPMCNT-400, and 20% Pt/C electrocatalysts. **b** The rotating disk electrode voltammograms of NPMCNT-300 electrocatalyst with different rotation speeds. **c** The Koutecky-Levich plots (*j* is the measured current density, *ω* is the angular velocity of the disk ($\omega = 2\pi N$, *N* is the linear rotation speed), **d** The rotating ring-disk electrode voltammograms, **e** the estimated value of electron transfer (*n*) and peroxide yields, and **f** the durability measurement of the NPMCNT-300 and Pt/C electrocatalysts

0.80, 0.89, 0.91, 0.90, 0.93, and 0.89 V (vs. RHE), respectively. Clearly, NPMCNT-300 exhibits the highest electrocatalytic activity. Compared with 40% Pt/C (0.993 V vs. RHE), the performance of former is slightly weaker, however, diffusion-limited current density for NPMCNT-300s is close to 6 mA cm^{-2}, which is better than Pt/C (5.1 mA cm^{-2}). Figure 4 b shows typical LSV curves for NPMCNT-300 at different various rotational speeds (from 625 to 2025 rpm). The value of electron transfer number for ORR process of NPMCNT-300 is calculated to be close to 4 when the potential is from 0.35 to 0.65 V, which confirms the four-electron transfer pathway (Fig. 4c). To estimate the ORR kinetics, the number of electron transfer and yield of H_2O_2 and were measured by RRDE method. The corresponding ring current is contemporaneously measured with a Pt ring electrode for detection of peroxide species at the disk electrode (Fig. 4d). The number of electron transfer (Fig. 4e) of the NPMCNT-300 was about 3.7, which is agree well with the reckoned data from K–L equation, indicating that the ORR process follows an efficient four-electron approach. In the presence of these electrocatalysts, the intermediate H_2O_2 formation rate is low, which is about 17%. In order to measure the stability of the electrocatalyst, we used the i-t method to characterize the electrocatalyst at a voltage of 0.5 V and the rotation speed of 1600 rpm in O_2-saturated 0.1 M KOH electrolyte. Figure 4 f shows the relative current density. After 40,000 s of continuous operation, NPMCNT-300 maintains a high relative current density of 94%, whereas, the initial current density was retained only 91% for Pt/C after continuous operation for 10,000 s, which indicates that the stability of NPMCNT-300 electrocatalyst is superior to the 40% Pt/C electrode.

To assess the electrocatalytic performance for OER of the NPMCNT-300, the LSV curves were tested at the scanning rate of 5 mV s^{-1}. In Fig. 5a, NPMCNT-300 electrocatalyst exhibits overpotential of 342 mV, which is equivalent to the potential of RuO_2 electrocatalyst (340 mV). While for NPMCNT, NPMCNT-50, NPMCNT-100, NPMCNT-200, and NPMCNT-400 were 579, 488, 461, 418, and 430 mV, respectively. Figure 5 b shows that the Tafel slope of NPMCNT-300 electrocatalyst is 74 mV dec^{-1} and for NPMCNT, NPMCNT-50, NPMCNT-100, NPMCNT-200, and NPMCNT-400 are 266, 170, 190, 137, 156 mV dec^{-1}, respectively. While the NPMCNT-300 electrocatalyst is lower than RuO_2 (88 mV dec^{-1}), therefore proving the excellent OER kinetics of NPMCNT-300 electrocatalyst. This results show that NPMCNT-300 has the excellent electrocatalytic performance as RuO_2 for OER. In order to investigate the durability of the NPMCNT-300 electrocatalyst, two methods were used. First, NPMCNT-300 was tested in a KOH electrolyte for 1000-cycle CV (Fig. 5c). After the test, it showed a little reduction in degradation (5 mV). Another stability test was using the chronoamperometry method. The chronoamperometry method is to record the change of current with time by applying a large step potential (from a potential jump occurring in a Faraday reaction to an effective potential approaching zero of the surface electroactive component of the electrode) to the working electrode in the unstirred solution. The initial potential was based on the results from Fig. 5d, which makes the NPMCNT-300 and RuO_2 to produced 10 mA cm^{-2} within iR compensation. The current of NPMCNT-300 electrocatalyst is retained for about 90% for 9 consecutive hours, while RuO_2 loses more than 50% of the current only in 1 h. Both stability tests indicate NPMCNT-300 has excellent stability for OER. Comparison of the electrocatalytic performance of CoP with various reported Co-based non-precious electrocatalysts in alkaline media in Table 1.

The above results summarize the corresponding OER and ORR electrochemical performances of different products, indicating that the intake of different phosphorus sources will affect the performance of the electrocatalysts. On one hand, although the electrocatalysts of NPMCNT-50, NPMCNT-100, and NPMCNT-200 have similar structures, the phosphorus content is lower which will cause the amount of CoP formation is less. On the other hand, although NPMCNT-400 contains the highest phosphorus content, due to the destruction of the original CNT structure, the CNTs clumped together and the electrocatalytic activity was relatively poor. The special morphology of NPMCNT-300 provides larger specific surface area as well as higher amount of CoP, resulting in improved electrochemical performance.

The electrochemically active surface area (ECSA) of the electrocatalysts can further indicate the cause of the excellent electrochemical activity. The double-layer capacitance (C_{dl}) of NPMCNT-50, NPMCNT-100,

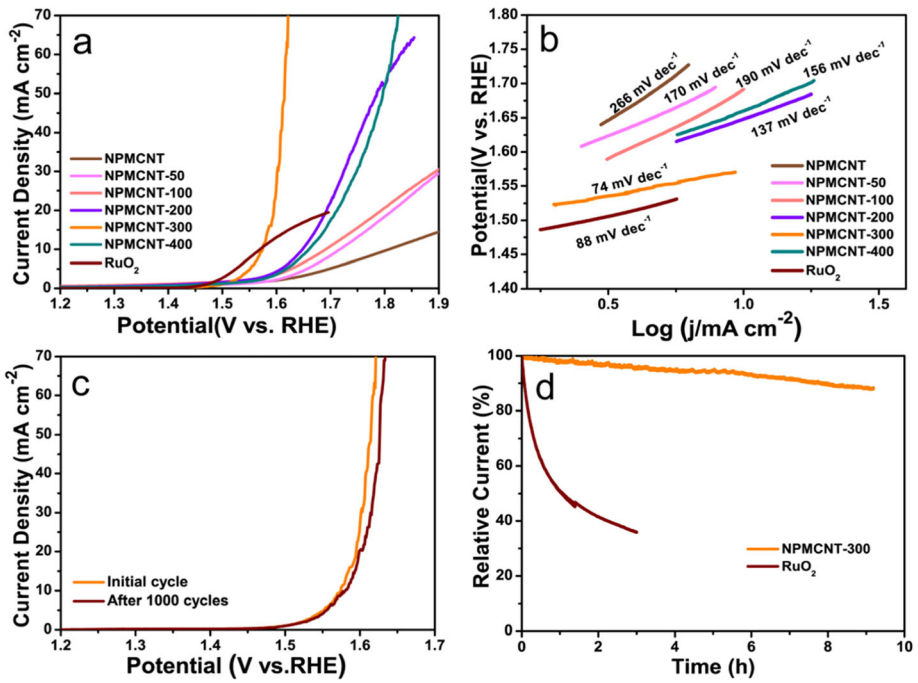

Fig. 5 **a** Linear sweep voltammetry curves of electrocatalysts with iR compensation. **b** Tafel plots of electrocatalysts calculating from Fig. **a**. **c** Linear sweep voltammetry curves for initial and after 1000 cycles cyclic voltammetry. **d** Amperometric i-t curves

Table 1 Comparison of the electrocatalytic performance of CoP with various reported Co-based non-precious electrocatalysts in alkaline media

Electrocatalyst	OER (η (mV) at j = 10 mA cm^{-2})	ORR ($E_{1/2}$ V)	Reference
Co_2P@NPC-1	327	0.83	[2]
NiP@N,P-CNSs	390	0.75	[7]
Co@N-CNTF	350	0.81	[11]
CoP NPs/CNSs	340	0.88	[60]
CoP-PBSCF	378	0.75	[61]
Bi–CoP/NP-DG	370	0.81	[62]
CoP_x/CoN_xC@CNT	460	0.83	[63]
CoNP@NC/NG-700	390	0.83	[64]
CoZn-NC-800	480	0.82	[65]
Co-N/C-800	492	0.67	[66]
Co/N-GCA	408	0.81	[67]
Co/CoP	**342**	**0.93**	**This work**

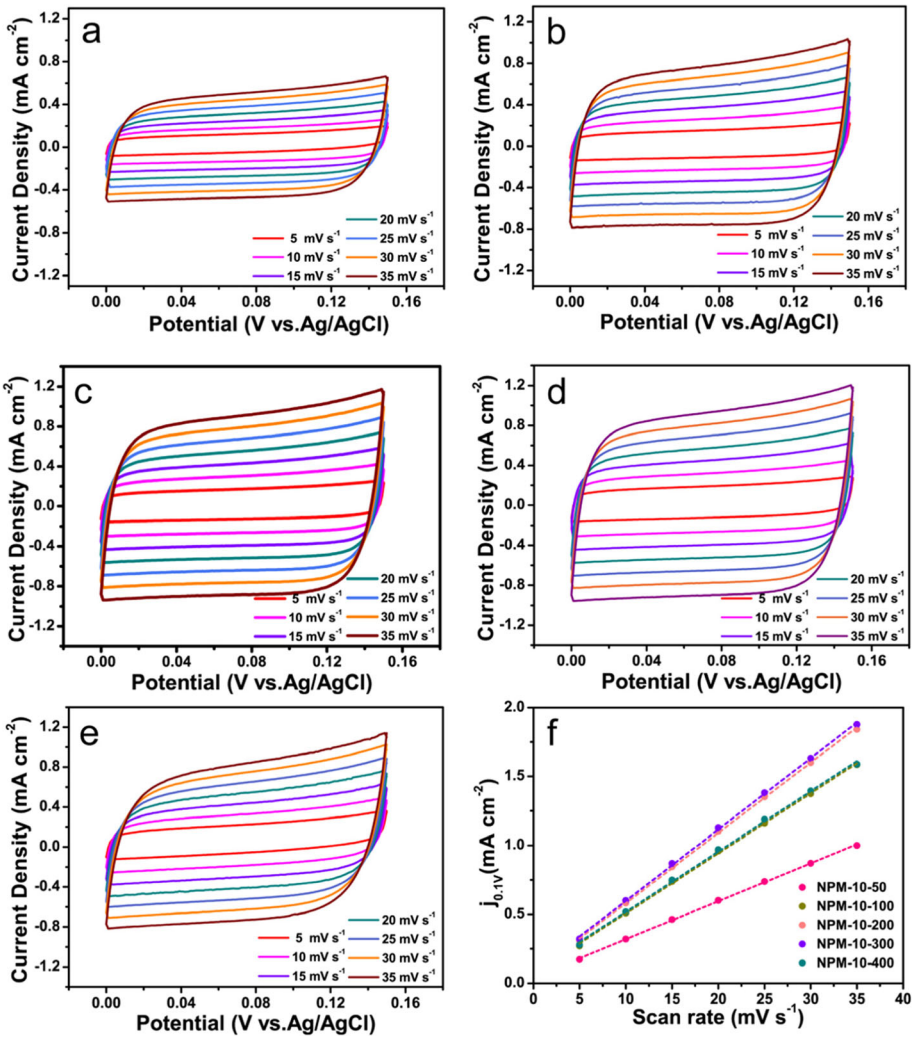

Fig. 6 Cyclic voltammetry scans of **a** NPMCNT-50, **b** NPMCNT-100, **c** NPMCNT-200, **d** NPMCNT-300, and **e** NPMCNT-400. **f** Plots between current density and scan rate for the electrocatalysts

NPMCNT-200 NPMCNT-300, and NPMCNT-400 was calculated at different various scan rates (0.005, 0.01, 0.15, 0.20, 0.25, 0.30, and 0.35 V s^{-1}) in Fig. 6a–e. In order to measure the electrochemical double-layer charge by CV, a potential range in which no significant Faraday process occurs is determined from the static CV. This range is typically a 0.1 V potential window centered at the open-circuit potential (OCP) of the system. All currents measured in this non-Faraday potential region are considered to be due to double-layer charging. Figure 6 f displays the plots between the various scan rates and the current density of the electrocatalyst at 0.1 V (vs. Ag/AgCl). The double-layer charging current is equal to the product of the scan rate, ν, and the electrochemical double-layer capacitance, C_{dl}, as given by Eq. (1):

$$ic = \nu C_{dl} \tag{13}$$

Thus, a plot of ic as a function of ν yields a straight line with a slope equal to C_{dl}. By plotting the Δj against the scan rate at 0.1 V (vs. Ag/AgCl), the slope which is twice of C_{dl} can be obtained as shown in Fig. 6f. The C_{dl} of linear fitting slope are 27.55, 43.55, 51, 51.75, and 43.73 mF cm^{-2} for NPMCNT-50, NPMCNT-100, NPMCNT-200, NPMCNT-300, and NPMCNT-400, respectively. The ECSA of a electrocatalyst sample is calculated from the C_{dl} according to Eq. (2):

$$\mathrm{ECSA} = C_{dl}/C_s \tag{14}$$

where Cs is the specific capacitance of the sample or the capacitance of an atomically smooth planar surface of the material per unit area under identical electrolyte conditions. By considering the specific capacitance of an atomically smooth planar surface with a real surface area of 1.0 cm^2, the specific capacitance (Cs) is generally within 20–60 μF cm^{-2} in alkaline media. For our estimates of surface area, we use general specific capacitances of Cs = 0.04 mF cm^{-2} in 0.1 M KOH. From this, we estimate that the ECSA are 0.0689, 0.1089, 0.1275, 0.1294, and 0.1093 m^2 for NPMCNT-50, NPMCNT-100, NPMCNT-200, NPMCNT-300, and NPMCNT-400 electrocatalysts. Therefore, the NPMCNT-300 electrocatalyst exhibits excellent performance for OER and ORR.

Conclusions

We make full use of the effective specific surface area of MOFs and high activity of CoP to produce excellent bifunctional electrocatalyst. The uniform introduction of cobalt sources on the surface of MOFs nanosheets by atomic layer deposition (ALD) techniques, and the derivation of N-doped nanotubes during high-temperature calcination, and encapsulation of Co/CoP in the tip of the nanotubes were reported. It is confirmed that the presence of nanotubes provides a larger specific surface area for the electrocatalyst. When used as a bifunctional electrocatalyst, NPMCNT-300 exhibits extraordinary electrochemical performance for both OER and ORR. It was demonstrating an onset-potential of 0.925 V for ORR and the overpotential is about 342 mV with a Tafel slope of 74 mV dec^{-1} for OER. Moreover, the electrocatalyst displayed prominent stability for both OER and ORR.

Abbreviations

OER: Oxygen evolution reaction; ORR: Oxygen reduction reaction; TMPs: Transition metal phosphides; CoP: Cobalt phosphide; MOFs: Metal-organic frameworks; CNTs: Carbon nanotubes; NPM: N-doped porous MOFs nanosheets; PE-ALD: Plasma-enhanced atomic layer deposition; XRD: X-ray diffraction; FESEM: Field emission scanning electron microscope; TEM: Transmission electron microscope; EDS: Energy dispersive X-ray spectroscopy; XPS: X-ray photoelectron spectroscopy; RRDE: Rotating ring-disk electrode; LSV: Linear sweep voltammogram; RHE: Reversible hydrogen electrode; K-L: Koutecky-Levich; ECSA: Electrochemical active surface area; CV: Cyclic voltammetry; C_{dl}: Double-layer capacitance

Authors' Contributions

YL conceived and designed the experiments. XY performed the experiments and analyzed the data. HM, XR, and PZ contributed the analysis tools. XY and YL wrote the paper. All authors read and approved the final manuscript.

Funding

This work was supported by the National Natural Science Foundation of China (no. 21878189), Shenzhen Science and Technology Project Program (no. KQJSCX20170327151152722), and the Natural Science Foundation of SZU (no. 827-000039).

Availability of Data and Materials

The datasets generated during and/or analyzed during the current study are available from the corresponding author on reasonable request.

Competing Interests

The authors declare that they have no competing interests.

Received: 18 October 2019 Accepted: 30 March 2020
Published online: 15 April 2020

References

1. Sun X, Yang X, Xiang H, Mi H, Zhang P, Ren X, Li Y, Li X (2019) Nitrogen-doped CoOx/carbon nanotubes derived by plasma-enhanced atomic layer deposition: efficient bifunctional electrocatalysts for oxygen reduction and evolution reactions. Electrochim Acta 296:964–971
2. Li J, Liu G, Liu B, Min Z, Qian D, Jiang J, Li J (2018) An extremely facile route to Co2P encased in N,P-codoped carbon layers: highly efficient bifunctional electrocatalysts for ORR and OER. Int J Hydrogen Energy 43:1365–1374
3. Sharma AK, Joshi H, Ojha K, Singh AK (2019) Graphene oxide supported cobalt phosphide nanorods designed from a molecular complex for efficient hydrogen evolution at low overpotential. Chem Commun (Camb). 55:2186–2189
4. Tian L, Yang T, Pu W, Zhang J (2019) Synthesis of cubic $Ni(OH)_2$ nanocages through coordinating etching and precipitating route for high-performance supercapacitors. Nanoscale Res Lett 14:264
5. Nandan R, Gautam A, Tripathi S, Nanda KK (2018) A comprehensive analysis and rational designing of efficient Fe-based oxygen electrocatalysts for metal–air batteries. J Mater Chem A 6:8537–8548
6. Xu J, Liu Y, Li J, Amorim I, Zhang B, Xiong D, Zhang N, Thalluri SM, Sousa JPS, Liu L (2018) Hollow cobalt phosphide octahedral pre-electrocatalysts with exceptionally high intrinsic catalytic activity for electro-oxidation of water and methanol. J Mater Chem A 6:20646–20652
7. Xiao Y, Deng S, Li M, Zhou Q, Xu L, Zhang H, Sun D, Tang Y (2019) Immobilization of Fe-doped Ni_2P particles within biomass agarose-derived

porous N,P-carbon nanosheets for efficient bifunctional oxygen electrocatalysis. Front Chem. 7:523
8. Fan Y, Wu Y, Huang X, Clavel G, Amsalem P, Koch N, Pinna N (2018) Polarization resistance-free Mn_3O_4-based electrocatalysts for the oxygen reduction reaction. ChemElectroChem. 5:2010–2018
9. Li C, Li X, Sun X, Zhang X, Duan L, Yang X, Wang L, Lu W (2019) Porous carbon networks derived from graphitic carbon nitride for efficient oxygen reduction reaction. Nanoscale Res Lett 14:249
10. Qian Y, Hu Z, Ge X, Yang S, Peng Y, Kang Z, Liu Z, Lee JY, Zhao D (2017) A metal-free ORR/OER bifunctional electrocatalyst derived from metal-organic frameworks for rechargeable Zn-Air batteries. Carbon 111:641–650
11. Guo H, Feng Q, Zhu J, Xu J, Li Q, Liu S, Xu K, Zhang C, Liu T (2019) Cobalt nanoparticle-embedded nitrogen-doped carbon/carbon nanotube frameworks derived from a metal–organic framework for tri-functional ORR, OER and HER electrocatalysis. J Mater Chem A 7:3664–3672
12. Lin Y, Yang L, Zhang Y, Jiang H, Xiao Z, Wu C, Zhang G, Jiang J, Song L (2018) Defective carbon-CoP nanoparticles hybrids with interfacial charges polarization for efficient bifunctional oxygen electrocatalysis. Adv Energy Mater 8:1703623
13. Guo C, Li Y, Xu Y, Xiang Q, Sun L, Zhang W, Li W, Si Y, Luo Z (2019) A highly nanoporous nitrogen-doped carbon microfiber derived from bioresource as a new kind of ORR electrocatalyst. Nanoscale Res Lett 14:22
14. Liu J, Liu Y, Li P, Wang L, Zhang H, Liu H, Liu J, Wang Y, Tian W, Wang X, Li Z, Wu M (2018) Fe-N-doped porous carbon from petroleum asphalt for highly efficient oxygen reduction reaction. Carbon 126:1–8
15. Zhong H, Wang J, Wang T, Zhang S, Li D, Tang P, Alonso-Vante N, Feng Y (2018) Surfactant-assisted fabrication of cubic cobalt oxide hybrid hollow spheres as electrocatalysts for the oxygen reduction reaction. Chem Electro Chem 5:2192–2198
16. Zhang X, Yang Z, Lu Z, Wang W (2018) Bifunctional CoN_x embedded graphene electrocatalysts for OER and ORR: a theoretical evaluation. Carbon 130:112–119
17. Zhang Y, Guo Y, Liu T, Feng F, Wang C, Hu H, Wu M, Ni M, Shao Z (2019) The synergistic effect accelerates the oxygen reduction/evolution reaction in a Zn-Air battery. Front Chem 7:524
18. Li J, Gui Y, Ji C, Tang C, Zhou Q, Wang Y, Zhang X (2018) Theoretical study of the adsorption of SF_6 decomposition components on Ni (111) surface. Computational Mater Sci 152:248–255
19. Liu D, Gui Y, Ji C, Tang C, Zhou Q, Li J, Zhang X (2019) Adsorption of SF_6 decomposition components over Pd (111): a density functional theory study. Appl Surf Sci 465:172–179
20. Wang Y, Gui Y, Ji C, Tang C, Zhou Q, Li J, Zhang X (2018) Adsorption of SF_6 decomposition components on Pt_3-TiO_2(1 0 1) surface: a DFT study. Appl Surf Sci 459:242–248
21. Du M, Qiu B, Zhu Q, Xing M, Zhang J (2018) Cobalt phosphide nanocages encapsulated with graphene as ultralong cycle life anodes for reversible lithium storage. Res Chem Intermediat 44:7847–7859
22. Pan Y, Sun K, Liu S, Cao X, Wu K, Cheong WC, Chen Z, Wang Y, Li Y, Liu Y, Wang D, Peng Q, Chen C, Li Y (2018) Core-shell ZIF-8@ZIF-67-derived CoP nanoparticle-embedded N-doped carbon nanotube hollow polyhedron for efficient overall water splitting. J Am Chem Soc 140:2610–2618
23. Mishra IK, Zhou H, Sun J, Qin F, Dahal K, Bao J, Chen S, Ren Z (2018) Hierarchical CoP/Ni_5P_4/CoP microsheet arrays as a robust pH-universal electrocatalyst for efficient hydrogen generation. Energy Environ Sci 11:2246–2252
24. Liu X, Li W, Zhao X, Liu Y, Nan CW, Fan LZ (2019) Two birds with one stone: metal–organic framework derived micro-/nanostructured Ni_2P/Ni hybrids embedded in porous carbon for electrocatalysis and energy storage. Adv Funct Mater 29:1901510
25. Mendoza-Garcia A, Zhu H, Yu Y, Li Q, Zhou L, Su D, Kramer MJ, Sun S (2015) Controlled anisotropic growth of Co-Fe-P from Co-Fe-O nanoparticles. Angew Chem Int Ed 54:9642–9645
26. Xu J, Li J, Xiong D, Zhang B, Liu Y, Wu KH, Amorim I, Li W, Liu L (2018) Trends in activity for the oxygen evolution reaction on transition metal (M = Fe, Co, Ni) phosphide pre-electrocatalysts. Chem Sci 9:3470–3476
27. Li W, Gao X, Xiong D, Xia F, Liu J, Song WG, Xu J, Thalluri SM, Cerqueira MF, Fu X, Liu L (2017) Vapor-solid synthesis of monolithic single-crystalline CoP nanowire electrodes for efficient and robust water electrolysis. Chem Sci 8:2952–2958
28. Duan J, Chen S, Vasileff A, Qiao SZ (2016) Anion and cation modulation in metal compounds for bifunctional overall water splitting. ACS Nano 10:8738–8745
29. Xu J, Xiong D, Amorim I, Liu L (2018) Template-free synthesis of hollow iron phosphide–phosphate composite nanotubes for sse as active and stable oxygen evolution electrocatalysts. ACS Appl Nano Mater 1:617–624
30. Ban J, Xu G, Zhang L, Xu G, Yang L, Sun Z, Jia D (2018) Efficient Co-N/PC@CNT bifunctional electrocatalytic materials for oxygen reduction and oxygen evolution reactions based on metal-organic frameworks. Nanoscale 10:9077–9086
31. Li D, Baydoun H, Kulikowski B, Brock SL (2017) Boosting the catalytic performance of iron phosphide nanorods for the oxygen evolution reaction by incorporation of manganese. Chem Mater 29:3048–3054
32. Xiong D, Wang X, Li W, Liu L (2016) Facile synthesis of iron phosphide nanorods for efficient and durable electrochemical oxygen evolution. Chem Commun (Camb) 52:8711–8714
33. Ganesan V, Kim J, Radhakrishnan S (2018) CoP embedded in hierarchical N-doped carbon nanotube frameworks as efficient electrocatalysts for the hydrogen evolution reaction. ChemElectroChem 5:1644–1651
34. Ma B, Yang Z, Chen Y, Yuan Z (2018) Nickel cobalt phosphide with three-dimensional nanostructure as a highly efficient electrocatalyst for hydrogen evolution reaction in both acidic and alkaline electrolytes. Nano Res 12:375–380
35. Lv Y, Wang X, Mei T, Li J, Wang J (2018) Reduced graphene oxide-supported cobalt phosphide nanoflowers via in situ hydrothermal synthesis as Pt-free effective electrocatalysts for oxygen reduction reaction. Nano 13:1850047
36. Li Y, Jia B, Chen B, Liu Q, Cai M, Xue Z, Fan Y, Wang HP, Su CY, Li G (2018) MOF-derived Mn doped porous CoP nanosheets as efficient and stable bifunctional electrocatalysts for water splitting. Dalton Trans 47:14679–14685
37. Li W, Zhao R, Zhou K, Shen C, Zhang X, Wu H, Ni L, Yan H, Diao G, Chen M (2019) Cage-structured MxPy@CNCs (M = Co and Zn) from MOF confined growth in carbon nanocages for superior lithium storage and hydrogen evolution performance. J Mater Chem A 7:8443-8450.
38. Shi W, Xu X, Ye C, Sha D, Yin R, Shen X, Liu X, Liu W, Shen J, Cao X, Gao C (2019) Bimetallic metal-irganic framework-derived carbon nanotube-based frameworks for enhanced capacitive deionization and Zn-Air battery. Front Chem 7:449
39. Su H, Zhou S, Zhang X, Sun H, Zhang H, Xiao Y, Yu K, Dong Z, Dai X, Huang X (2018) Metal-organic frameworks-derived core-shell Fe_3O_4/Fe_3N@graphite carbon nanocomposites as excellent non-precious metal electrocatalyst for oxygen reduction. Dalton Trans 47:16567–16577
40. Wang Z, Yu H, Han J, Xie G, Chen S (2017) Rare Co/Fe-MOFs exhibiting high catalytic activity in electrochemical aptasensors for ultrasensitive detection of ochratoxin A. Chem Commun (Camb) 53:9926–9929
41. Wang Q, Liu Z, Zhao H, Huang H, Jiao H, Du Y (2018) MOF-derived porous Ni2P nanosheets as novel bifunctional electrocatalysts for the hydrogen and oxygen evolution reactions. J Mater Chem A 6:18720–18727
42. Liu T, Li P, Yao N, Cheng G, Chen S, Luo W, Yin Y (2019) CoP-doped MOF-based electrocatalyst for pH-universal hydrogen evolution reaction. Angew Chem Int Ed 58:4679–4684
43. Wu F, Zhang S, Xi B, Feng Z, Sun D, Ma X, Zhang J, Feng J, Xiong S (2018) Unusual formation of CoO@C "dandelions" derived from 2D Kagóme MOLs for efficient lithium storage. Adv Energy Mater 8:1703242
44. Wu YP, Zhou W, Zhao J, Dong WW, Lan YQ, Li DS, Sun C, Bu X (2017) Surfactant-sssisted phase-selective synthesis of new cobalt MOFs and their efficient electrocatalytic hydrogen evolution reaction. Angew Chem Int Ed 56:13001–13005
45. Dou S, Li X, Tao L, Huo J, Wang S (2016) Cobalt nanoparticle-embedded carbon nanotube/porous carbon hybrid derived from MOF-encapsulated Co_3O_4 for oxygen electrocatalysis. Chem Commun (Camb) 52:9727–9730
46. Jiang H, Gu J, Zheng X, Liu M, Qiu X, Wang L, Li W, Chen Z, Ji X, Li J (2019) Defect-rich and ultrathin N doped carbon nanosheets as advanced trifunctional metal-free electrocatalysts for the ORR, OER and HER. Energy Environ Sci 12:322–333
47. Ghosh S, Basu RN (2018) Multifunctional nanostructured electrocatalysts for energy conversion and storage: current status and perspectives. Nanoscale 10:11241–11280
48. Wei H, Gui Y, Kang J, Wang W, Tang C (2018) A DFT study on the adsorption of H_2S and SO_2 on Ni doped MoS_2 monolayer. Nanomaterials 8:646
49. Li H, Xu SM, Yan H, Yang L, Xu S (2018) Cobalt phosphide composite encapsulated within N,P-doped carbon nanotubes for synergistic oxygen evolution. Small 14:e1800367

50. Zhu M, Zhou Y, Sun Y, Zhu C, Hu L, Gao J, Huang H, Liu Y, Kang Z (2018) Cobalt phosphide/carbon dots composite as an efficient electrocatalyst for oxygen evolution reaction. Dalton Trans 47:5459–5464
51. Zhu J, Ren Z, Du S, Xie Y, Wu J, Meng H, Xue Y, Fu H (2017) Co-vacancy-rich $Co_{1-x}S$ nanosheets anchored on rGO for high-efficiency oxygen evolution. Nano Res 10:1819–1831
52. Li H, Ke F, Zhu J (2018) MOF-derived ultrathin cobalt phosphide nanosheets as efficient bifunctional hydrogen evolution reaction and oxygen evolution reaction electrocatalysts. Nanomaterials (Basel) 8:89
53. Li F, Bu Y, Lv Z, Mahmood J, Han GF, Ahmad I, Kim G, Zhong Q, Baek JB (2017) Porous cobalt phosphide polyhedrons with iron doping as an efficient bifunctional electrocatalyst. Small 13:1701167
54. Li R, Wei Z, Gou X (2015) Nitrogen and phosphorus dual-doped graphene/carbon nanosheets as bifunctional electrocatalysts for oxygen reduction and evolution. ACS Catal 5:4133–4142
55. Yu X, Zhang S, Li C, Zhu C, Chen Y, Gao P, Qi L, Zhang X (2016) Hollow CoP nanopaticle/N-doped graphene hybrids as highly active and stable bifunctional electrocatalysts for full water splitting. Nanoscale 8:10902–10907
56. Wang T, Kou Z, Mu S, Liu J, He D, Amiinu IS, Meng W, Zhou K, Luo Z, Chaemchuen S, Verpoort F (2018) 2D dual-metal zeolitic-imidazolate-framework-(ZIF)-derived bifunctional air electrodes with ultrahigh electrochemical properties for rechargeable zinc-air batteries. Adv Funct Mater 28:1705048
57. Jiang Y, Deng YP, Fu J, Lee DU, Liang R, Cano ZP, Liu Y, Bai Z, Hwang S, Yang L, Su D, Chu W, Chen Z (2018) Interpenetrating triphase cobalt-based nanocomposites as efficient bifunctional oxygen electrocatalysts for long-lasting rechargeable Zn-Air batteries. Adv Energy Mater 8:1702900
58. Park J, Risch M, Nam G, Park M, Shin TJ, Park S, Kim MG, Shao-Horn Y, Cho J (2017) Single crystalline pyrochlore nanoparticles with metallic conduction as efficient bi-functional oxygen electrocatalysts for Zn–air batteries. Energy Environ Sci 10:129–136
59. Torad NL, Hu M, Kamachi Y, Takai K, Imura M, Naito M, Yamauchi Y (2013) Facile synthesis of nanoporous carbons with controlled particle sizes by direct carbonization of monodispersed ZIF-8 crystals. Chem Commun (Camb) 49:2521–2523
60. Zou W, Dou K, Jiang Q, Xiang J, Kaun C-C, Tang H (2019) Nearly spherical CoP nanoparticle/carbon nanosheet hybrids: a high-performance trifunctional electrocatalyst for oxygen reduction and water splitting. RSC Adv 9:39951–39957
61. Zhang Y, Tao H, Chen Z, Li M, Sun Y, Hua B, Luo J (2019) In situ grown cobalt phosphide (CoP) on perovskite nanofibers as an optimized trifunctional electrocatalyst for Zn–air batteries and overall water splitting. J Mater Chem A 7:26607–26617
62. Chen J, Ni B, Hu J, Wu Z, Jin W (2019) Defective graphene aerogel-supported Bi–CoP nanoparticles as a high-potential air cathode for rechargeable Zn–air batteries. J Mater Chem A 7:22507–22513
63. Wu X, Chen S, Feng Y, Yuan Q, Gao J, Chen Y, Huang Y, He Y, Gan W (2019) Microwave-assisted synthesis of carbon nanotubes threaded core-shell CoP_x/Co-N-x-C@CNT and its performance as an efficient bifunctional oxygen electrocatalyst for the rechargeable zinc-air battery Materials. Today Physics 9:100132
64. Zhong X, Jiang Y, Chen X, Wang L, Zhuang G, Li X, Wang J (2016) Integrating cobalt phosphide and cobalt nitride-embedded nitrogen-rich nanocarbons: high-performance bifunctional electrocatalysts for oxygen reduction and evolution. J Mater Chem A 4:10575–10584
65. Chen BH, He XB, Yin FX, Wang H, Liu DJ, Shi RX, Chen JN, Yin HW (2017) MO-Co@N-doped carbon (M = Zn or Co): vital roles of inactive Zn and highly efficient activity toward oxygen reduction/evolution reactions for rechargeable Zn-air battery. Adv Funct Mater 27:14
66. Xu G, Xu GC, Ban JJ, Zhang L, Lin H, Qi CL, Sun CL, Jia DZ (2018) Cobalt and cobalt oxides n-codoped porous carbon derived from metal-organic framework as bifunctional electrocatalyst for oxygen reduction and oxygen evolution reactions. J Colloid Interf Sci 521:141–149
67. Qiao X, Jin J, Fan H, Cui L, Ji S, Li Y, Liao S (2018) Cobalt and nitrogen co-doped graphene-carbon nanotube aerogel as an efficient bifunctional electrocatalyst for oxygen reduction and evolution reactions. Catal 8:275

Publisher's Note